Engineering Structures 245 (2021) 112952

Contents lists available at ScienceDirect

Engineering Structures

journal homepage: www.elsevier.com/locate/engstruct

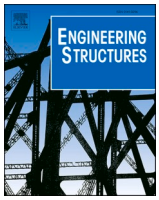

Influence of large-scale asperities on the shear strength of concrete-rock interface of small buttress dams

Gabriel Sas [a], Cosmin Popescu [b,*], Dipen Bista [a,c], Andreas Seger [a], Bård Arntsen [a], Fredrik Johansson [d], Leif Lia [c]

[a] SINTEF Narvik AS, Narvik 8517, Norway
[b] Luleå University of Technology, Luleå 971 87, Sweden
[c] Norwegian University of Science and Technology (NTNU), Trondheim 7491, Norway
[d] Royal Institute of Technology (KTH), Stockholm 10044, Sweden

A B S T R A C T

This paper presents an investigation of the influence of large-scale asperities on the shear strength of four physical models of a pillar (also known as buttress web) from Kalhovd dam in Norway. The objective was to observe the structural behaviour of the pillar under design and ultimate loading scenarios and to compare results of the tests with those of nonlinear finite element analysis (FEA) and standard guideline methods. Four models at 1:5 scale were prepared with different interface profiles and tested. The results from model test and the results of a benchmarking process carried out with nonlinear FEA are presented. Furthermore, the FEA was expanded to other hypothetical scenarios to extend understanding of effects of the locations and inclinations of large-scale asperities on the sliding stability of concrete dams. The results are compared with those obtained using standard design methods and estimated safety factors are presented.

1. Introduction

Numerous small concrete dams (lower than 15 m), are ageing and many are reaching their design lifetime. Moreover, many of them were designed to meet lower safety requirements than those present today. Therefore, many are deemed unstable, resulting in costly upgrading and repairs.

Sliding along the concrete rock interface is a potential failure scenario that should be evaluated in any safety assessment of concrete dams. A combination of the Limit Equilibrium Method (LEM) and Mohr-Coulomb (M−C) failure criterion is currently the most widely used method to verify the sliding stability of existing concrete dams [1–3]. The method involves simplified treatment of the concrete rock interface of a dam as a set of rectilinear planes corresponding to pre-set possible failure paths, to determine its sliding resistance and a corresponding safety factor.

The M−C criterion assumes that the shear strength is governed by the cohesive (c) and the frictional resistance (ϕ) of the surfaces in contact. Due to high uncertainties associated with the existence and distribution of bonding between rock and concrete, cohesion is often neglected [1,4–6] in sliding assessments. The frictional resistance is the sum of the basic friction angle (an intrinsic property) and roughness component, but these two effects are not decoupled in the M−C criterion. Roughness can be quantified as first-order roughness or waviness (in a meter or decimetre scale), and second-order roughness or unevenness (in centimetre or millimetre scale) [7]. Although the first order roughness (large scale asperities or shear keys) determines the overall behaviour of an interface [7–9], the LEM does not account for contributions of their locations along a dam's interface.

The influence of roughness on the shear strength of rock joints has been extensively studied both experimentally and theoretically [4,8–17]. Nevertheless, as highlighted by a recent review by Thirukumaran and Indraratna [18], there are considerable uncertainties in the prediction accuracy of shear strength models empirically derived from laboratory tests under constant normal loading (CNL) conditions.

In addition, there have been far fewer investigations of dams' concrete-rock interfaces [5], partly at least because concrete-rock interfaces are regarded as a subcategory of rock-rock joints [19]. However, concrete-rock joints of dams have considerably greater shear strength than rock-rock joints tested in similar conditions [20] due to differences in their nature and morphology. Rock joints are planes of weakness in rock masses caused by past geological processes, while for many dams the interfaces are prepared by blasting [21], which results in roughness of different scales and amplitudes than joints in rock masses. For a blasted surface, these large-scale asperities are highly irregular, with large amplitudes and large inclinations against the shear direction. Typical amplitudes range between 0.3 and 0.5 m depending on the blasting technique [22].

* Corresponding author.
E-mail address: cosmin.popescu@ltu.se (C. Popescu).

https://doi.org/10.1016/j.engstruct.2021.112952
Received 15 September 2020; Received in revised form 12 June 2021; Accepted 2 August 2021
Available online 20 August 2021

Many of today's conclusions are based on, or corroborated by, evidence from laboratory tests. However, the validity of predicting the shear strength of an entire dam interface based on small-scale laboratory joints is debatable because of potential scale effects [23,24]. The peak shear strength obtained from laboratory testing only represents the strength associated with second-order roughness. Hence, it does not truly capture the effect of large-scale asperities at the decimetre or meter scale [25]. In practice, direct application of laboratory-derived scale relationships can produce unrealistic results, so there have been a number of attempts to counter this problem. According to Barton and Bandis [26], as the scale is increased the geometrical component (i) changes from second order roughness, with i values often in the range of 40 to 50°, to first order roughness with implicit reductions in shear strength. To account for this reduction Barton and Bandis [27] subsequently proposed an empirical equation based on extensive experimental testing. However, application of the scaling equations to any scale larger than about 2 m reduces the roughness component of shear strength to unrealistically low values [22]. Ladanyi and Archambault [28] proposed a model for the progressive change from dilation to shearing through the asperities, but the final form of the equation did not gain wide acceptance due to its complexity and limited experimental validation. Alternative peak shear strength criteria based on a function of frictional and dilation components have been suggested, with the dilation component defined as the maximum asperity angle at a normal stress, small enough to guarantee that deformations of the asperities will be negligible [29]. Furthermore, it has also been suggested that the scale effect does not necessarily exist but is rather an effect of the degree of matedness of the joint [30]. Combining large scale waviness and small scale roughness into a single term to describe joint conditions has also been proposed [31,32]. However, these alternative approaches do not consider effects of scale at relevant magnitudes for dams' foundations. Thus, a methodology to account for the shear strength of entire dam interfaces still requires refinement [22], and a robust approach is likely to involve multiscale assessment combining advanced scanning measurements of topography, small-scale laboratory tests and numerical modelling [33].

In a recent study [34], the effects of asperities' locations along the interface on the shear strength of unbonded small concrete-rock joints were investigated. Tests conducted under direct and eccentric shear loading conditions revealed significant variations in shear capacity and failure modes of the concrete-rock joints depending on the location of the large scale asperity under eccentric loading.

To extend the practical engineering value of the cited findings by Bista et al. [34], this paper reports results of an experimental and numerical campaign carried out on physical models of a pillar (buttress web) in a real flat slab buttress concrete dam. The objective was to investigate how large-scale asperities with different dilation angles and locations contribute to the shear strength of unbonded concrete-rock interfaces. The results are compared with values obtained for a sample with a flat interface (replicating cases with limit equilibrium analysis assumptions). Potential implications for dam safety are discussed.

2. Kalhovd dam

2.1. Description and previous safety investigations

Kalhovd Dam is a small concrete buttress dam (Fig. 1) in Norway. The 386 m long dam, of which 140 m is free spillway, was built during 1940–1948. It has 66 pillars with heights of 1.5–13.3 m and 5 m distance between their centres. The rock foundation is mainly composed of diorite gneiss type rock. A reassessment of structural safety, based on current Norwegian regulations [35], indicated that 32 sections of the dam do not fulfil the safety criteria against sliding. Field activities included scanning of the entire dam using 3D laser technology and material sampling by core drilling. The 3D scanning generated a highly accurate digital model of the dam's geometry and topography of the foundation, which revealed large discrepancies in assumptions used in the standardized assessment process.

Properties of the concrete and rock obtained by subjecting cores extracted from the dam site to mechanical tests, are summarized in Table 1. For further details see Sas et al. [36].

3. Methods

3.1. Model tests

3.1.1. Design of experiments

The conceptual design of the samples was based on the following considerations. First, scale effects should be avoided, and since a full-scale test of a monolith of a dam is unfeasible due to lack of resources, we decided to conduct tests on scaled-down samples, i.e. geomechanical models. Second, the test setup should represent the forces acting on the dam as realistically as possible.

Fig. 1. Overview of Kalhovd dam.

Table 1
Mechanical properties of prototype materials (Mean and covariance (CoV)) vs target mechanical properties of model materials and design loads of prototype dam vs target design load of model.

		Prototype		Model
		Mean	CoV	Mean
Concrete	Cylinder Comp. strength [MPa]	41.2	27%	8.2
	Cube Comp. strength [MPa]	33	27%	
	Tensile strength [Mpa]	4	20%	0.8
	Elastic modules [GPa]	26.3	18%	5.2
	Avg. strains (80% peak strength)	0.00053	15%	
	Strain at crushing	0.0013	13%	0.002
	Friction angle [deg]	36.2	6%	36.2
	Density [kg/m^3]	2354		2354
Rock	Compressive strength [Mpa]	86.7	44%	17.3
	Tensile strength [Mpa]	10.4	27%	2.1
	Elastic modules [Gpa]	46	27%	6.7
	Friction angle [deg]	28.5	8%	28.5
	Poisson's ratio	0.2		0.2
Loads	Ice pressure [kPa]	200		40
	Hydrostatic pressure [kPa]	61.1		12.2
	Max. Uplift [kPa]	61.1		12.2

One of the 32 pillars with identified insufficient stability, pillar 49 (Fig. 2), was selected for a case study. This pillar has two distinct asperities at points approximately one and two thirds along the interface that were not accounted for in the reassessment. In addition to its low sliding resistance, this pillar was selected for the following three reasons. First, from a practical engineering perspective, tests could potentially show that current theoretical methods substantially underestimate the real capacity of such sections. Small-scale tests [34] have shown that the location of an asperity along an interface strongly influences its contributions to strength. Therefore, it was important to determine if these results were replicable at a larger scale. The second reason for choosing the selected pillar is that it provided opportunities to test effects of varying the inclination of a potential failure plane. This was deemed important for highlighting the subjective nature of the choice of this plane in practical engineering calculations. Typically, a potential sliding plane is chosen by joining two extreme points, often the upstream–downstream extremities in analytical calculations. In the selected case, a potential sliding plane would have an average inclination of −4.4°with respect to a horizontal plane, but other configurations can also be selected, as illustrated in Fig. 2, which would yield different results. The third reason for selecting the pillar is that the profile includes two asperities with different inclinations along a potential failure plane, providing opportunities to assess contributions of both their locations along the plane and their inclination.

The original drawings of the dam show that the reinforcement ratio in the pillars is so low that it should make negligible contribution to structural capacity of the sections according to current structural engineering standards. Therefore, unreinforced specimens were manufactured.

Since the only varied parameter was the topographical profile it was deemed sufficient to solely produce samples of the pillar, hence the plate was disregarded.

3.1.2. Scaling laws and properties of models

The samples were scaled down 1:5, using similitude theory [37] to establish the necessary and sufficient conditions of similarity between the prototype (real structure) and models (specimens). Testing of subscale models is a well-established and widely used destructive physical analysis technique in engineering [37], and has been extensively applied to investigate dams' stability [38–42]. The models constructed in this study could be classified as "design models", used "to help verify calculations for very large and monumental structures where failure consequences could be extremely serious" [37]. Similarity criteria were applied to the loads, geometry and material properties. Derivations of the criteria and properties are described elsewhere [36], and they are related through the following equations:

$$\frac{S_\sigma}{S_L S_\rho} = 1, \tag{1}$$

$$S_\varepsilon = S_\rho = S_\nu = 1, \tag{2}$$

$$\frac{S_\sigma}{S_E} = \frac{S_\sigma}{S_L} = \frac{S_\sigma}{S_f} = 1 \tag{3}$$

Here, symbol S denote the scaling factor and the symbols L, ρ, s, E, ν, ε, σ, and f denote the geometry, density, displacement, modulus of elasticity, Poisson's ratio, stress, strain and strength parameters, respectively. Based on these scaling laws the geometry relation, $S_L = 1/5$, between the prototype and models was established according to Table 1.

3.1.3. Construction of model pillars

Four samples were created with different topographical profiles (Fig. 3). Each sample consisted of one pillar and one foundation. Pillars and foundations were created at separate times. First the foundations were cast using a ready mixed concrete material. The foundation consisted of two parts, the base and the profile. Transversal sections are shown in Fig. 3.

The base of the foundation was reinforced with four bars of 12 mm diameter in longitudinal direction and stirrups of 6 mm diameter with 100 mm spacing to avoid cracking during installation in test setup and loading. The contour of the profiles was created simultaneously with the base of the foundation by match casting against custom-made polystyrene formworks.

The geometry of the pillars reproduced in detail the main features of the prototype (section 49), including the door (Fig. 3).

The thickness of the prototype pillar varies over the height. However, the model pillars were constructed with a constant average thickness of 100 mm. Each pillar was horizontally match-cast against each profile. Bonding between the newly cast material and hardened foundation was prevented by spraying the foundation with rubber paint. For each sample, 10 cylinders and six cubes were cast at the same time as the sample. The cubes and cylinders were tested during the day when the corresponding sample was tested. Mechanical properties of the materials are reported in Table 2.

Samples were named with reference to the positions of the two main asperities along the interface. The naming of the samples consists of the following: U and D refer to the Upstream and Downstream asperities, respectively, while 37° and 16° refer to the inclination of the face of the asperity against the sliding direction. In addition, in some subsequent designations T and F indicate real (tested) and simulated (Finite Element Analysis) samples.

One sample, named U-16°-D-37° was designed to have an accurate 2D representation of the original profile of section 49 (Fig. 2). Two others, named D-37° and U-16°, had identical profiles except that they respectively lacked the upstream and downstream asperities. The last sample, named R, lacked both asperities (the bottom of its profile was simply created by joining the upstream and downstream points). Second and higher order roughness was ignored to avoid coupling effects of first and higher order roughness, and associated complications in assessments of the effects of the losses of asperities in samples D-37°, U-16° and R.

3.1.4. Development of material for model pillars

The material used to create the model pillars was a micro-concrete modified iteratively from a commercial cement-based dry mortar powder in efforts to obtain the desired scaled strength values (Table 1). The final mix was 1 part cement, to 0.6 part water and 3 parts sand (0–4 mm). The ingredients were mixed for 15 min until a homogeneous cementitious admixture was obtained. Then, each model was cast from a single batch together with cylinders and cubes for standard testing of material properties. The friction angle was determined through tilt angle tests [43]. Pairs of concrete cubes from foundations and cubes from each model pillar were subjected to two sets of tests. In the first set the plain

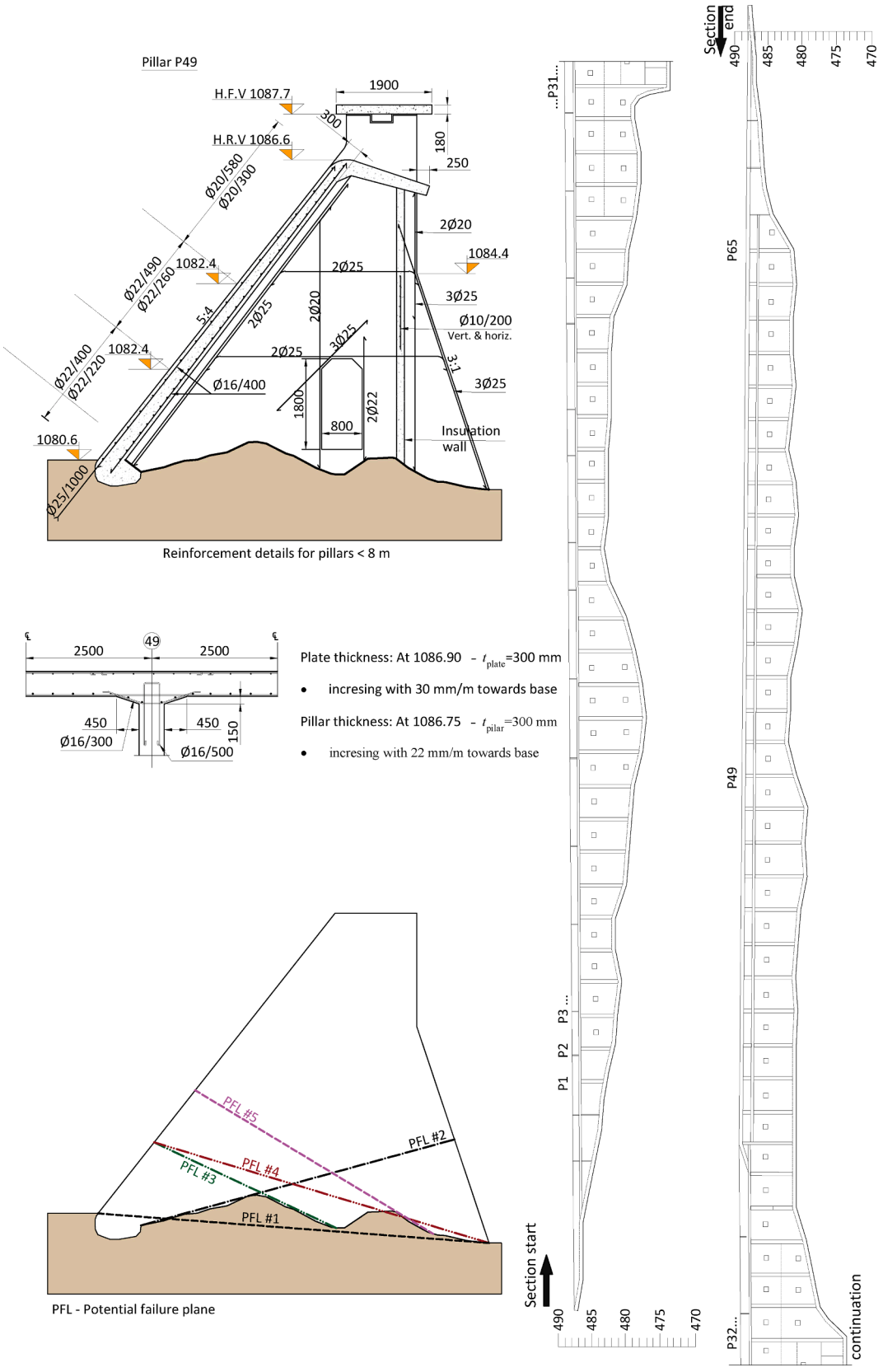

Fig. 2. Overview of the dam, the reinforcement detailing and geometry of pillar 49, and potential assumed failure planes.

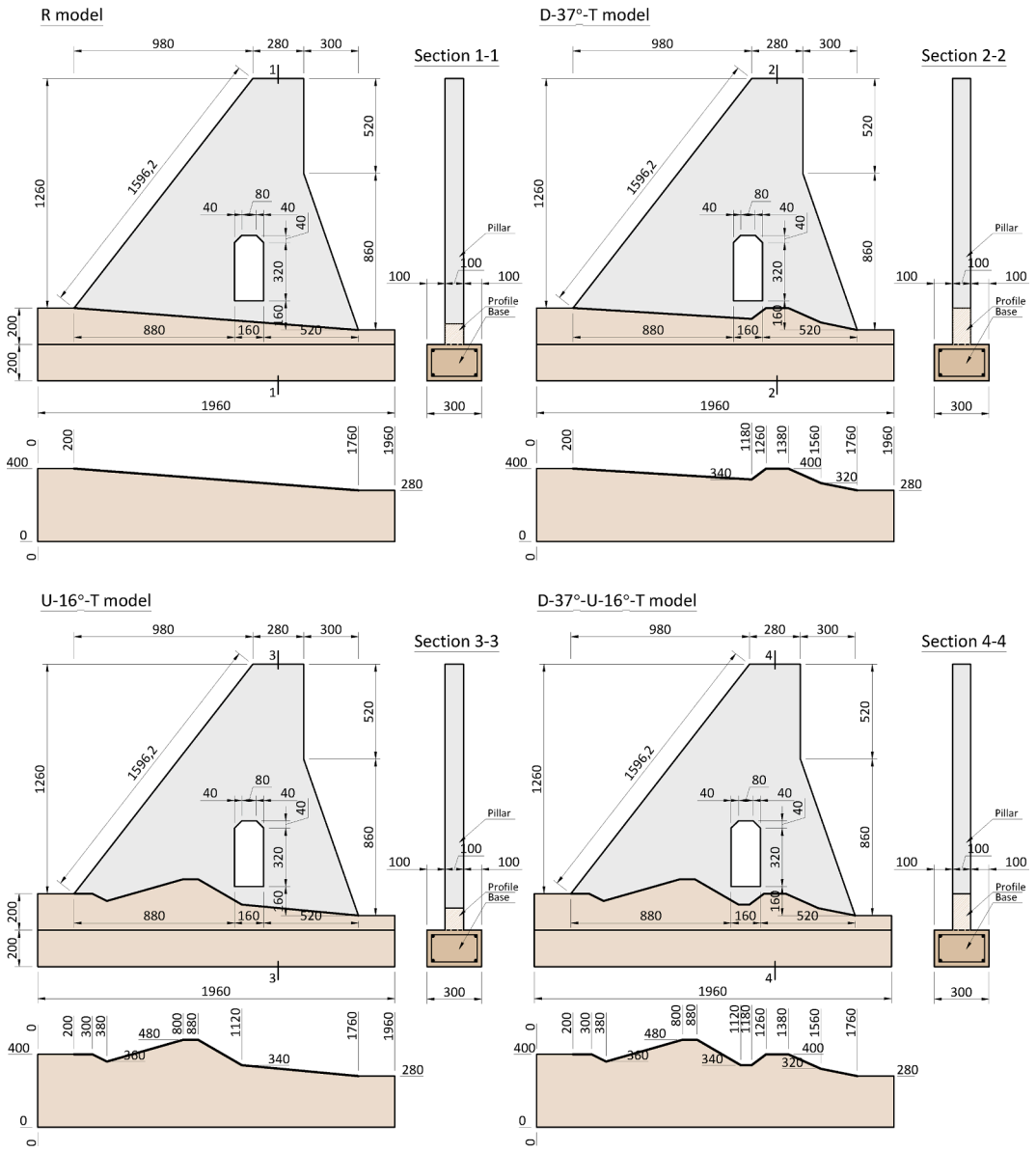

Fig. 3. The geometry of the produced samples.

Table 2
Mechanical properties of model materials used to construct pillars and deviations (%-diff. Target) from those of original materials.

Model test		Compressive strength	Tensile strength	Friction angle		Secant modulus	Strain ε_c (‰) at:		
				rough samples	brushed samples				
		$f_{c,cyl}$ (MPa)	f_t (MPa)	ϕ_p	ϕ_s	E_c (GPa)	Onset of crushing	80% of peak	Peak
Targeted values		8.0	0.8	36.2	–	5.2	0.2	–	–
R	Measured	11.1	1.2	37.9	32.0	10.9	0.3	1.4	3.1
	% -diff. Target	27.9 %	30.7 %	4.4 %	–	52.3 %	20.0 %	–	–
D-37°	Measured	7.9	0.8	35.6	32.7	8.3	0.4	1.1	2.0
	% -diff. Target	−1.7 %	−1.3 %	−1.7 %	–	37.2 %	49.2 %	–	–
U-16°	Measured	9.4	0.8	36.1	32.5	9.6	0.3	1.1	2.3
	% -diff. Target	15.2 %	1.0 %	−0.3 %	–	45.8 %	35.5 %	–	–
U-16°-D-37°	Measured	10.0	0.8	35.6	30.7	10.1	0.2	1.1	2.5
	% -diff. Target	20.3 %	0.0 %	−1.6 %	–	48.5 %	18.9 %	–	–

concrete cubes were used, and in the second set the cubes were sprayed with the rubber paint used to prevent bonding between the foundation and models. The paint was then scraped off with a steel brush; then, the friction angle was measured again. The intention was to determine the influence of the surface preparation on the frictional properties.

3.1.5. Test setup and loading sequence

The test setup consisted of a loading system and a guiding system (Fig. 4).

The loading system was designed to replicate the scaled hydrostatic pressure, uplift pressure and ice pressure. In this paper only tests related to the hydrostatic loading pressure are reported, other tests involving overturning actions are reported elsewhere[36].

The hydrostatic pressure was simulated by two inclined loading actuators, P1 and P2, exerting pressure through a loading beam (Fig. 4). The loading beam, together with the position and inclination of the actuators, was selected to create the desired distributed loading along the pillar's face. A pressure film was placed between the loading beam and pillar in the pilot test to confirm the pressure distribution. Total load was applied at a rate of 2.4 kN/min. The load cells were servo controlled and was pre-programmed where the two actuators, P1 and P2, always apply 55% and 45% respectively of the total applied load. This ensured a triangular pressure distribution of the applied load.

An additional 40 kg weight was added to the pillar to compensate for the difference in density between the prototype and model materials, and for geometric deviations between the original and model pillars.

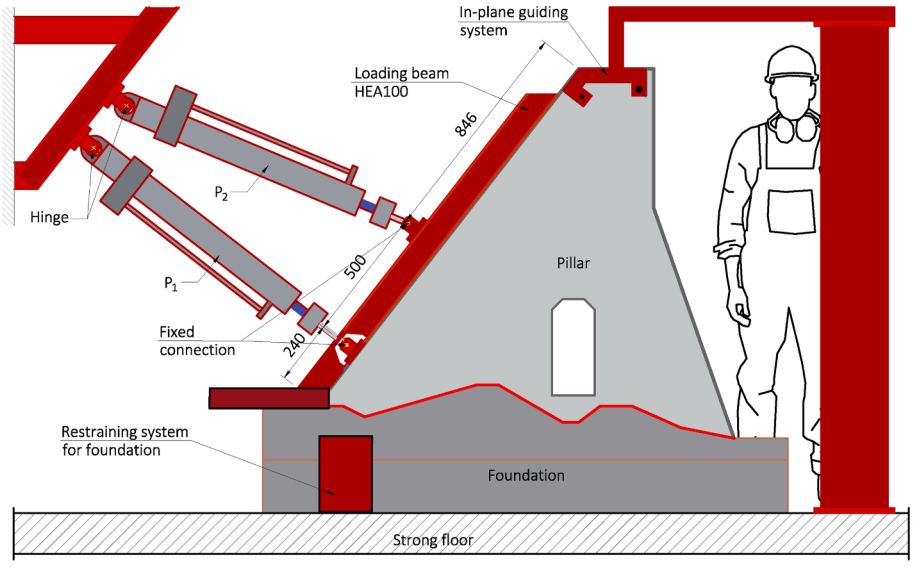

(A)

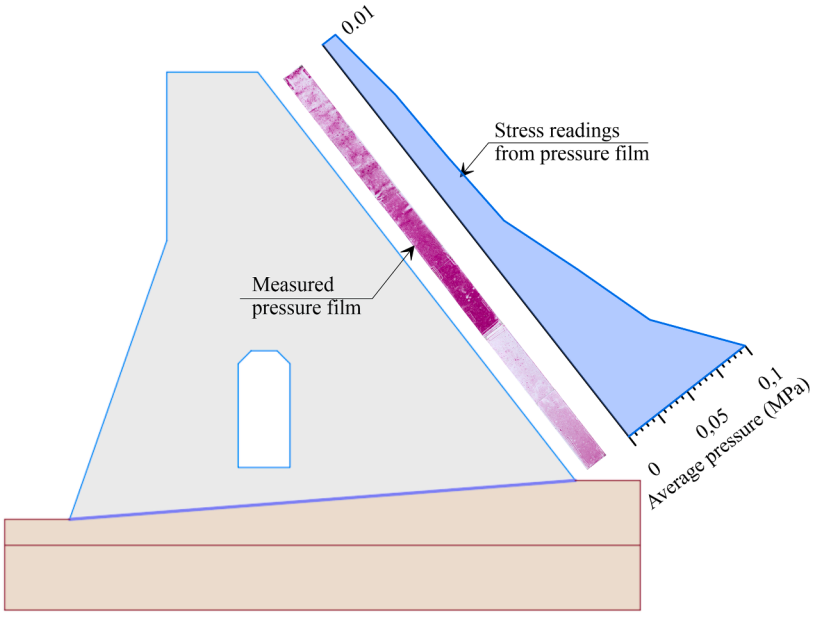

(B)

Fig. 4. Schematic diagram of: (a) the test setup and (b) stress distribution as measured by the pressure film.

The test setup was designed so that it would not restrain in-plane rotation of the sample while loading increased. The loading procedure consisted of increasing the loading in nominal steps. The first corresponded to the hydrostatic pressure exerted by the highest regulated water level in the dam. If failure did not occur, higher loads were added until failure. Any extra loads applied above the nominal value (highest regulated water level) were considered as overloading. Loads were applied continuously in load-controlled increments and between loads the loading process was paused to allow proper distribution of forces in the sample.

3.1.6. Instrumentation and monitoring

The samples' behaviour under loading was monitored by optical, photogrammetric 3D measurements (Fig. 5). In photogrammetry, a series of images is recorded using digital cameras, and coordinates of points (targets), patterns, and features in the images are subsequently identified using image-processing techniques [44]. In this study, both Digital Image Correlation (DIC) and point-tracking methods were used to monitor the behaviour of the tested specimens in real-time. In contrast to point-tracking, where displacement is recorded at only a handful of points, the DIC technique involves full-field monitoring of surfaces prepared by applying a high-contrast (usually black and white) speckle pattern, ideally stochastic. Images of prepared specimens' surfaces in initial undeformed and later deformed stages, are acquired to obtain deformation (strain) data. In this study, each specimen was imaged at a frequency of 2 Hz using a 5 M system configuration [45].

In addition, horizontal and vertical displacements were monitored using linear displacement sensors (LVDTs) at positions indicated in Fig. 5, which provided backup system for the optical measurement system and data, confirming that no significant movement of the foundation occurred.

3.2. Finite element analysis

3.2.1. Scope of simulations

The main objective of the FEA simulations was to investigate effects of changing locations of the asperities. The numerical analysis was conducted with ATENA commercial software [46]. The process was carried out in two stages. First the model tests were simulated. In this process, aspects such as boundary conditions, mesh size and integration methods were calibrated so that the results would correspond to those of the model tests in terms of failure modes and load displacement (with 10% tolerance) based on the guidelines of [47].

In the second stage three hypothetical cases were simulated by changing locations of the asperities in the U-16°-D-37°-T to U-37°-D-16°-F, D-37°-T to U-37°-F and U-16°-T to D-16°-F in finite element models.

3.2.2. Modelling strategy

The specimens were modelled in 2D with a mesh of 8-node serendipity plane stress finite elements. A Gaussian integration scheme with 2 × 2 integration points was used for all the concrete elements. Mesh quality was determined after sensitivity analysis of the consistency of the results with respect to computational time. An example of a FE model with mesh and boundary conditions is shown in Fig. 6. The incremental and iterative Arch Length method for material nonlinear structural analysis was used in the numerical simulations, based on the finite element method.

3.2.3. Material models

3.2.3.1. Concrete. The constitutive model for concrete used in the analysis is a fracture-plastic model that combines constitutive submodels for tensile and compressive behaviour, as presented in the

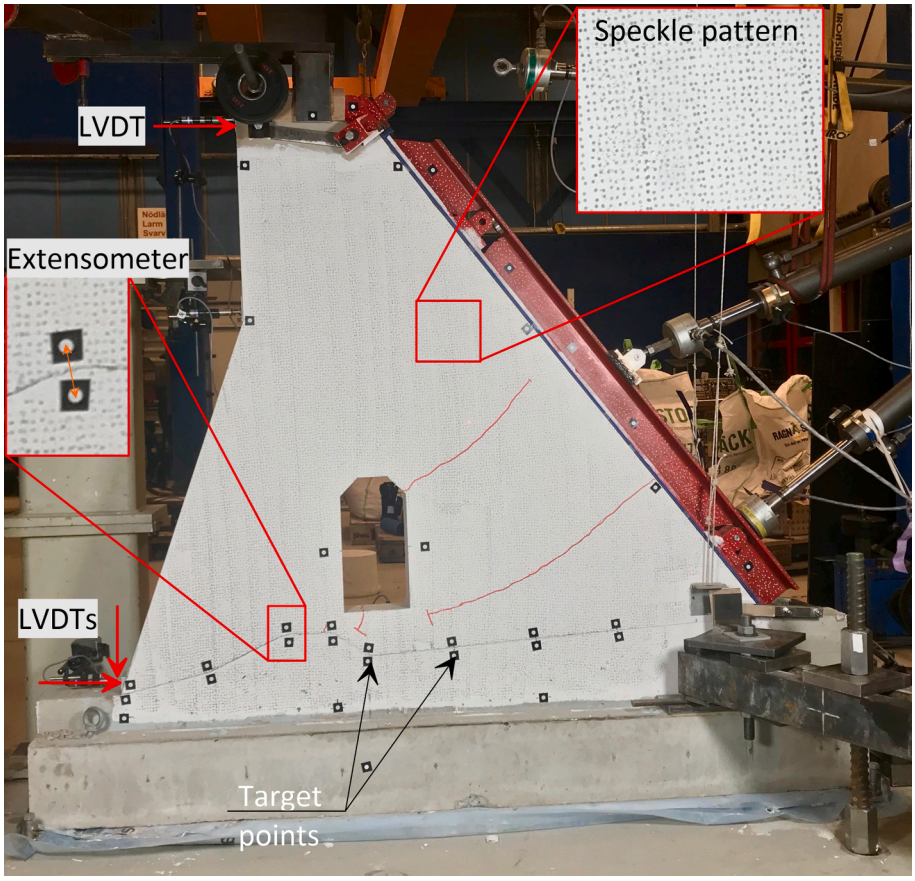

Fig. 5. Image of the test setup showing the speckle pattern applied for the DIC monitoring.

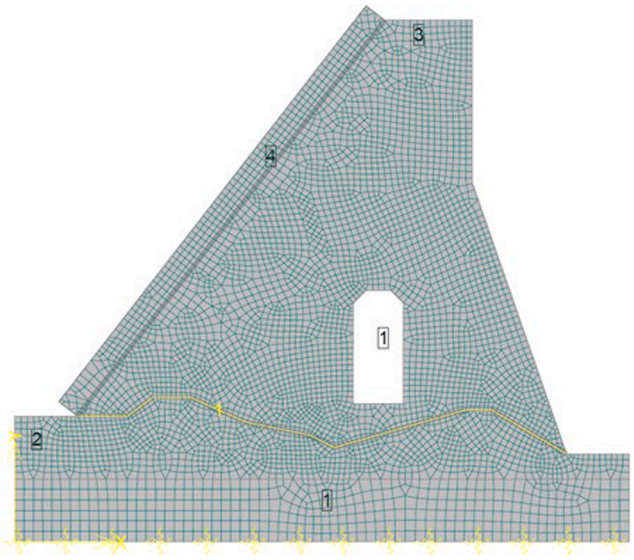

Fig. 6. FE model of U-37-D-16-F sample with mesh and boundary conditions.

ATENA user manual [46]. The fracture model employs the Rankine failure criterion and exponential softening. The concrete's post-cracking tensile behaviour was simulated by the softening function illustrated in Fig. 7 in combination with the crack band theory.

The default fracture energy used in ATENA is derived for standard concrete with regular aggregate size. The mortar used in these tests had a maximum aggregate size of 4 mm, which is small compared to standard concretes. Therefore, values of the fracture energy were calculated using the equation by Pan et al. [48] that directly relates the fracture energy to the aggregate size (Fig. 7).

The hardening/softening plasticity model is based on the Menétrey-Willam failure surface, using a return-mapping algorithm for the integration of constitutive equations. The plasticity model is combined with the fracture model by an algorithm based on recursive substitution. This approach allows the two models to be formulated and developed separately.

3.2.3.2. Pillar-foundation interface. The behaviour of the simulated interface material is based on the Mohr-Coulomb criterion with tension cut off (Fig. 8). The constitutive relation is given in terms of tractions on interface planes and relative sliding and opening displacements (Equation (4))

$$\begin{Bmatrix} \tau \\ \sigma \end{Bmatrix} = \begin{bmatrix} K_{tt} & 0 \\ 0 & K_{nn} \end{bmatrix} \begin{Bmatrix} \Delta v \\ \Delta u \end{Bmatrix} \tag{4}$$

The initial failure surface corresponds to the Mohr-Coulomb condition with ellipsoid in tension regime (Fig. 8). After stresses violate this

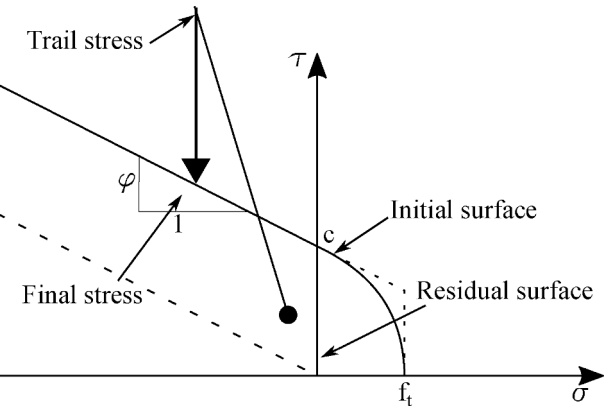

Fig. 8. Mohr-Coulomb failure surface for interface elements implemented in ATENA.

condition, the surface collapses to a residual surface, which corresponds to residual friction.

K_{nn} and K_{tt} denote the initial elastic normal and shear stiffness, respectively, estimated as the ratios E/t and G/t, where *E* and *G* are the elastic and shear modulus, respectively of the weakest material in the interface (here, concrete), and *t* is the width of the interface zone.

3.2.4. Loads and boundary conditions

The loads were applied on the load beam as point loads. Since the FE model is a 2D model, a beam of the same geometry cannot be created. Hence, the beam was modelled by a beam with rectangular cross section and the same moment of inertia (I_{xx} = 349.2 cm^4) as HEA 100 [49].

The interface between the loading beam and the pillar was modelled as a Mohr-Coulomb interface, curve fitted to the displacement response measured in tests. During the experiment, the foundation block is resting on the strong floor. A thin layer of gypsum was used between the foundation block and the floor to level it horizontally. It was kept in place (to avoid lateral movement and any rotation due to lateral loads) through the steel yokes which may affect its stiffness. Hence, the stiffness provided by this fixing system and gypsum layer had to be calibrated in order to capture the correct behavior of the entire model test.

4. Results

The results are presented in terms of maximum load resisted, displacement at maximum load and failure mechanism of the tested and simulated models. Fig. 9 presents the overall structural behaviour of the samples in terms of load displacement graphs obtained from the model tests and finite element analysis. The results of the finite element analysis show a very good correlation to those from the model tests, in terms of both load displacement behaviour and failure modes. Slight differences

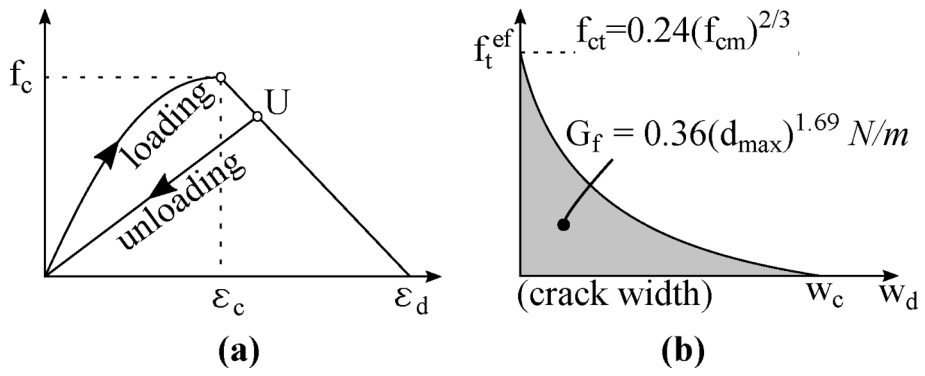

Fig. 7. Constitutive material models for (a) concrete compressive hardening/softening; (b) exponential crack opening law.

Table 3
Summary of results from model tests and FE-analysis.

Sample	Failure mode	Failure load (kN)	% of design load	% increase with respect to reference case (R-T)	Onset of sliding (kN)	Friction angle (°)[a]
Test						
R-T	sliding	4.4	47%		3.2	45.6
U-16-T	sliding	9.2	99%	110%	4.1	53.2
D-37-T	crack	50.7	545%	1052%	–	61.5
U-16-D37-T	crack	37.2	400%	745%	–	60.9
FEM (Benchmarking)						
R-F(B)	sliding	3.1	33%		3.0	
U-16-F(B)	sliding	8.7	94%	98%	5.5	53.4
D-37-F(B)	crack	54.9	590%	1148%	–	61.6
U-16-D37-F(B)	crack	40.2	432%	813%	–	61.1
FEM (parametric)						
D-16-F	sliding	17.5	189%	299%	16.7	58.1
U-37-F	crack	7.8	84%	77%	–	52.4
U-37-D-16-F	crack	17.5	188%	297%	–	58.3

[a] back-calculated by Mohr-Coulomb criterion (cohesion = 0).

were noted in the load capacity of the samples that failed through diagonal cracking in the pillar concrete. These differences may have been due to the idealized nature of the numerical simulations and variations in materials in the physical model that were not accounted for. The results of both model tests and simulations are summarized in Table 3.

4.1. Results of model tests

The R-T sample failed at an applied total load of 4.4 kN, 47% of the nominal hydrostatic pressure. The displacement vectors shown in Fig. 10 are all aligned in the same direction, showing that the sample behaved as a rigid body up to failure. Deformations of the foundation and the asperity were extremely small. Sliding was sudden and not perceived with the naked eye. The maximum force was recorded at about 0.6 mm relative displacement at the top of the pillar (Fig. 9).

The U-16°-T sample failed at an applied total load of 9.2 kN, corresponding to 99% of the design value of hydrostatic pressure through sliding. At maximum force, the relative displacement recorded at the top of the pillar was 4.7 mm (Fig. 9). The displacement vectors calculated from the DIC measurements (Fig. 11) show that under hydrostatic loads the pillar had a tendency to slide along all planes of the interface, thus acting as a rigid body. However, the directions of the vectors were not parallel to each individual plane. Close to failure, the toe of the dam was significantly loaded too, showing the presence of rotation of the entire sample due to rigid body movement.

The D-37°-T sample failed at a total load of 50.7 kN, corresponding to 4.5 times more hydrostatic pressure than the design value of 9.3 kN. The directions of displacement vectors calculated from the DIC measurements (Fig. 12) at increments of the design hydrostatic pressure show a general tendency of downwards movement, indicating a tendency to slide along all planes of the interface. Failure was recorded when the loads suddenly dropped, and the displacement excessively increased. The maximum force was recorded at about 0.8 mm relative displacement at the top of the pillar. The mode of failure consisted of diagonal cracking through the pillar model (Fig. 13). The principal strains plotted at loads at failure and after failure (Fig. 13) reveal that failure could also have occurred through another crack that started at the corner of the door opening. The two cracks were almost parallel and aligned towards the face of the loaded side of the asperity. In addition, post-failure inspection showed that local crushing of the concrete between the left corner of the door and the asperity occurred on about two thirds of that area, indicating that the sample was also close to a compressive failure.

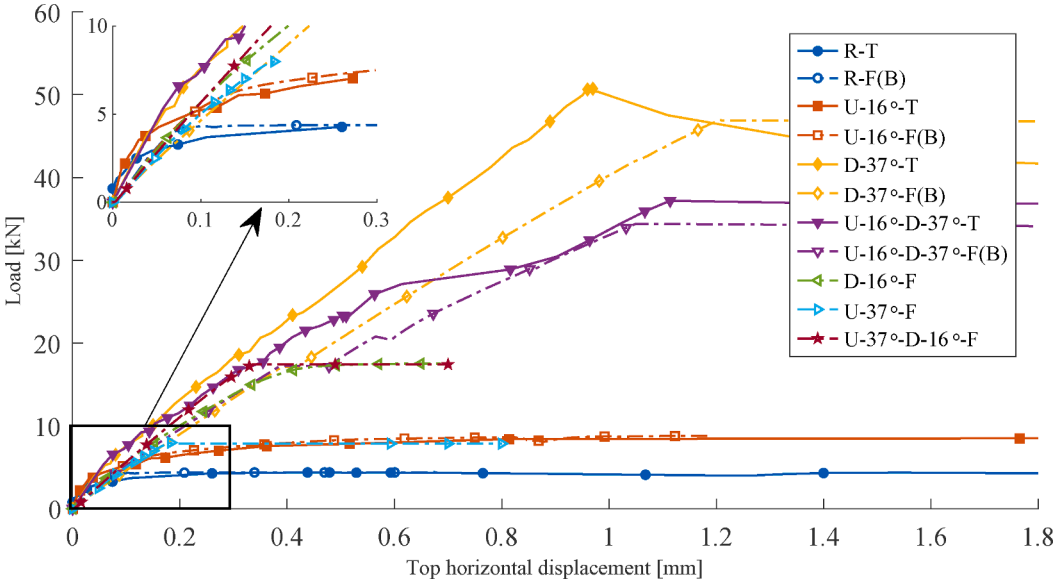

Fig. 9. Load displacements of indicated samples recorded in the sliding tests (solid line, name ends with- T) and numerical analysis (dash-solid line, names end with –F or –F(B) for the numerical analysis of the tests.).

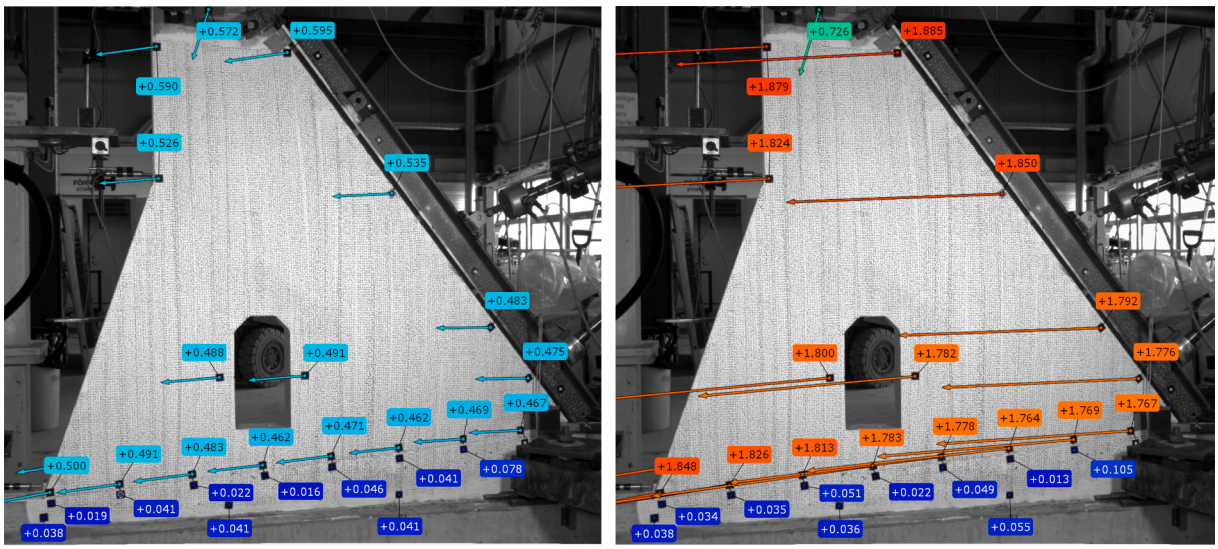

a) b)

Fig. 10. Displacement vectors for the sample R-T at (a) failure load and (b) after sliding failure.

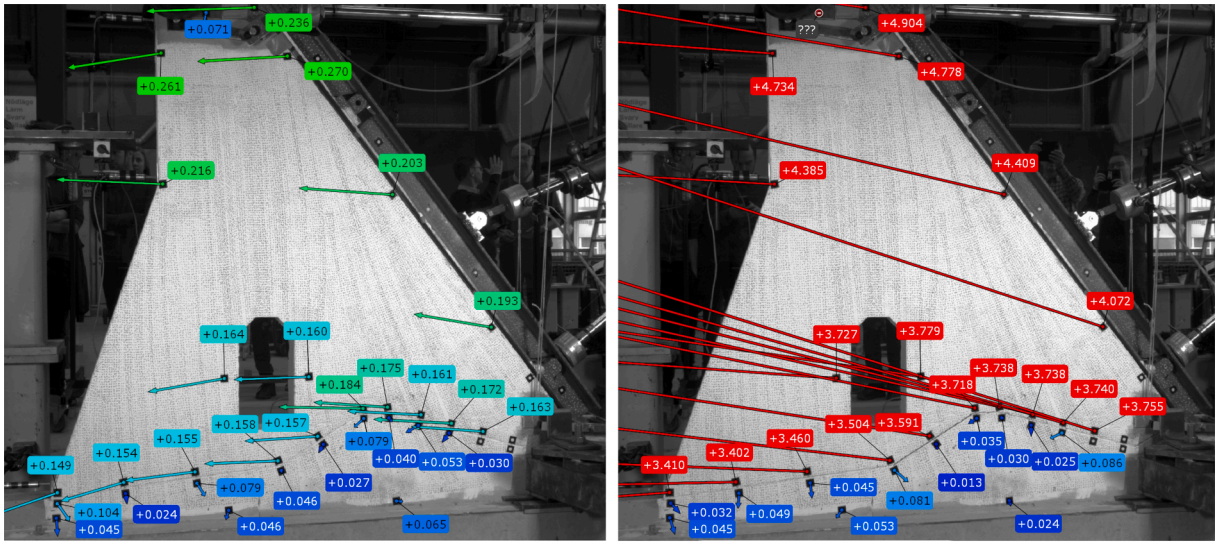

a) b)

Fig. 11. Displacement vectors for the U-16°-T sample at (a) 75% of failure load and (b) after failure.

The U-16°-D-37°-T sample failed at a total load of 30.2 kN, corresponding to three times more hydrostatic pressure than the design value of 9.3 kN. The behaviour of this sample was similar to that of the D-37°-T sample. The directions of displacement vectors calculated from the DIC measurements (Fig. 14) at increments of the design hydrostatic pressure show a general tendency of downwards movement, indicating a tendency to slide along all planes of the interface. Failure was recorded when the loads suddenly dropped, and the displacement excessively increased. The maximum force was recorded at about 0.9 mm relative displacement at the top of the pillar. The mode of failure consisted of diagonal cracking through the pillar (Fig. 15 c). The principal strains plotted at loads approaching failure and after failure (Fig. 13) show that the crack was perpendicular to the loading direction and parallel to the unloaded face of the first asperity. The plots also show that both asperities contributed to the resistance mechanism, mainly through their faces oriented against the sliding direction, the downstream asperity being more loaded than the upstream asperity.

4.2. Results from finite element analysis

The D-16°-F sample failed at an applied total load of 17.5 kN by sliding over the asperity (Fig. 9 and Fig. 19). This failure mode was similar to that observed in sample U-16°-T. However, the failure load for D-16°-F was almost 2-fold more than that of U-16-T, corresponding to 190 % of the design value of hydrostatic pressure. The maximum force was observed at 0.7 mm relative displacement recorded at the top of the pillar (Fig. 9). The displacement vectors calculated by the ATENA software (Fig. 16) show a rigid body movement similar to that of U-16°-T. However, the directions of the vectors are not parallel to each individual plane.

The U-37°-F sample failed at a total load of 7.8 kN, corresponding to just a sixth of the load borne by the D-37°-T sample and 84% of the design hydrostatic load. The maximum force was recorded at about 0.2 mm relative displacement at the top of the pillar. The mode of failure consisted of diagonal cracking through the pillar between the lower load cell and the asperity (Fig. 19). The directions of displacement vectors

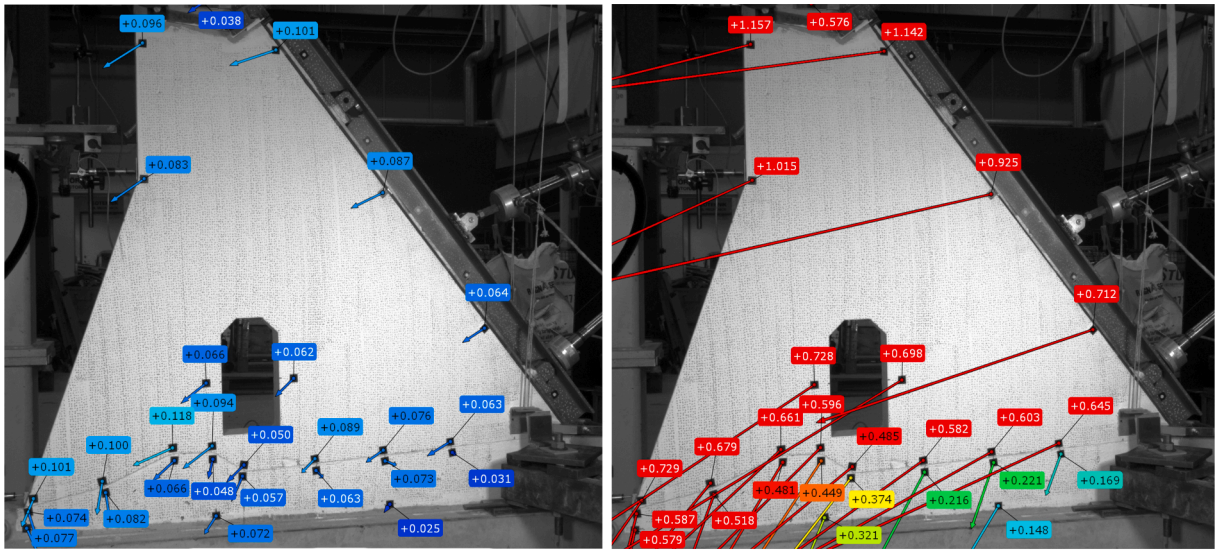

a) b)

Fig. 12. Displacement vectors for the D-37°-T sample at (a) 75% of failure load and (b) after failure.

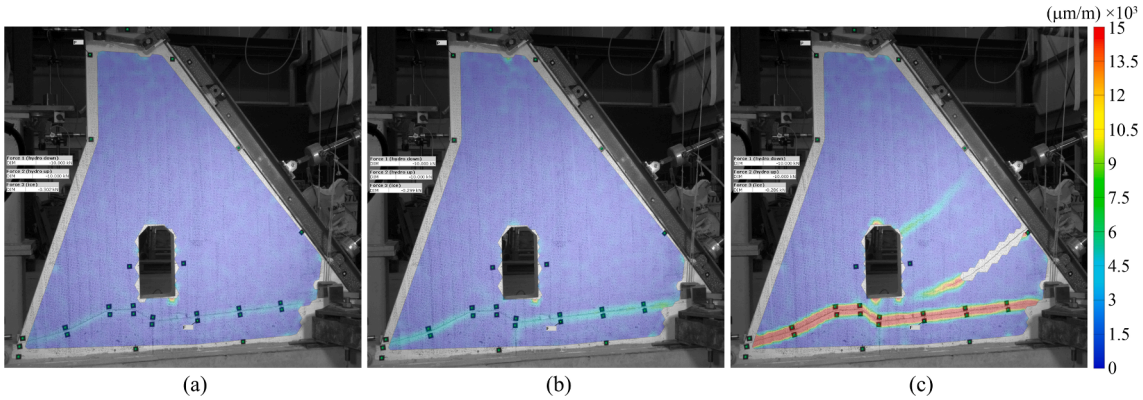

(a) (b) (c)

Fig. 13. Principal strains in D-37°-T at (a) 75% of failure (b) 100% of failure and (c) after failure.

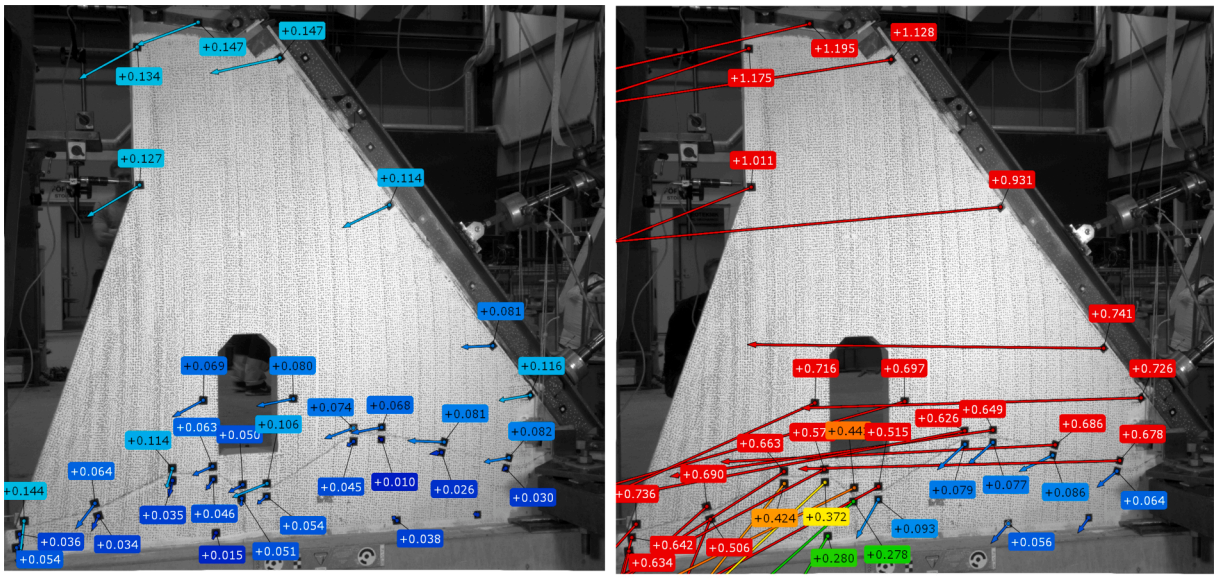

a) b)

Fig. 14. Displacement vectors for the U-16-D-37°-T sample at (a) 75% of failure load and (b) after failure.

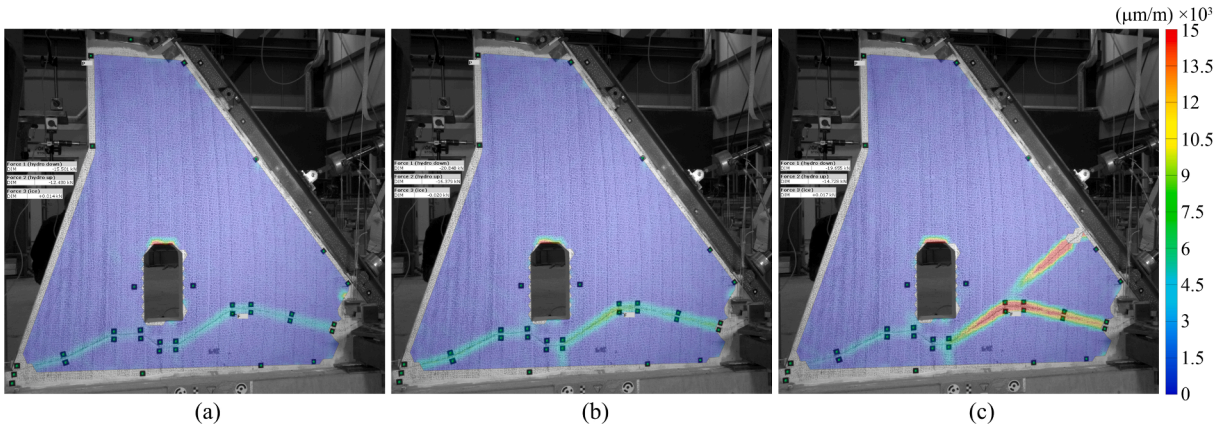

Fig. 15. U-16-D-37°-T Principal strains at (a) 75% of failure; (b) 100% of failure and (c) after failure.

calculated by the ATENA software (Fig. 17) show differences in vector lengths within the pillar, indicating differential movement of pillar concrete. The pillar in front of the asperity was displaced the least, indicating an interlocking effect at the asperity. The interlocking effect can also be seen in Fig. 20 (e) where the compressive strains at the concrete rock interface of the samples were plotted.

The U-37°-D-16°-F sample failed at a total load of 17.5 kN, corresponding to only about half of the load borne by the U-16°-D-37°-T sample and 190% of the design hydrostatic load. The maximum force was recorded at about 0.34 mm relative displacement at the top of the pillar. Like U-37°-F, the U-37°-D-16°-F sample failed by diagonal cracking in the pillar concrete (Fig. 19). failure load for U-37°-D-16°-F was about 2-fold more than that of U-37°-F. This was because the downstream asperity in U-37°-D-16°-F was also taking the applied stresses, unlike in U-37°-F, where most stresses were transferred through the asperity. Hence, more load was required to reach the failure stresses in the U-37°-D-16°-F sample.

The displacement vectors calculated by the ATENA software (Fig. 18) have a similar pattern to that obtained for the U-37-F sample. The vectors suggest differential displacement occurred within the pillar, with the concrete in front of the asperity being displaced the least, indicating an interlocking effect of the asperity at the front.

5. Analysis and discussion

The following analysis and discussion are based on results of the tests and numerical analysis, focusing on contributions of the asperities to the overall shear strength of the interface of the pillars.

5.1. Samples with failure through concrete

The load displacement diagrams in Fig. 9 show that the samples that failed through concrete cracking in the pillar (U-16-D-37°-T, D-37°-T, U-37°-F, U-37°-D16° -F), exhibited linear load displacement behaviour up to failure. The failure had a distinct pattern, causing irreversible damage in the pillars. No damage was observed in the foundation or asperities. Notably, all samples with a steep asperity (37°) failed in this mode, regardless of the asperity's location (upstream or downstream) and configuration of the interface (single or multiple asperities). This indicates that interlocking between the pillar and asperity may occur beyond a certain angle (~30°) as previously proposed Johansson and Stille [4]. These results are consistent with those of tests on unbonded concrete-rock joints conducted in laboratory conditions on samples with triangular asperities [34]. Direct shear tests under different normal loads performed on samples with asperities with angles lower than 30° tend to fail by sliding [50,51], while those with asperities with higher angles fail by fracture within the asperity or in the concrete dam body [50,52]. This failure mode is not covered in typical assessment procedures for plate dams. This failure type resembles that of concrete surface elements (such as walls or high beams) loaded in their own plane. Thus, an appropriate model based on strut and tie or concrete plasticity theories could potentially be adapted from existing models of laterally loaded disks to cover this failure mode.

5.2. Samples with sliding failure

On the other hand, for samples R-T, D-16°-F and U-16°-T, it is not straight forward when sliding failure occurred. Load displacement responses of these samples started to be nonlinear at loading stages before the failure load (Table 3). This can be considered to be the onset of the process of sliding. As the loads increased, the non-linearity increased too, until maximum resistance was reached. However, this resistance was reached later (e.g. for the U-16-T sample at about 8 kN, Table 3), and up to this point the samples were already significantly displaced through progressive sliding, manifested by an increasingly visible gap between the pillar and the foundation. Nevertheless, failure occurred suddenly, accompanied by a loud sound and drop in load.

5.3. Influence of asperity on shear strength

Table 3 also shows that the presence of asperities increases the shear capacity of an otherwise planar interface (like reference sample R-T), but with high variation, depending on both the location of the asperity and inclination angle of the face against the loading direction.

Results for the samples with single asperities (Table 3 and Fig. 20) indicate that asperities located downstream (as in samples D-16-F and D-37-T) contribute more to the shear strength than those located upstream (as in samples U-16-T, U-37-F). Samples U-37-D-16-F and U-37-F also had lower capacity than samples U-16-D37-T and U-16-T. Thus, a steep asperity located upstream seems to have an early interlocking effect, providing support (Fig. 20). In this sense the external forces are transmitted to the asperity via the shortest path, through concrete, in the form of diagonal compression fields. This is also in accordance with the results in [34].

The presence of two asperities in an interface, as in U-16-D37-T and U-37-D-16-F, does not necessarily confer higher capacity than a single asperity (Table 3). The first asperity, closest to the loads, seems to govern the pillar's initial behaviour. Comparison of results obtained for samples U-16-T and U-16-D37-T indicate that in the latter sliding occurred over the upstream, gentler asperity until the interlocking provided by the steeper downstream asperity restrained the sample's movement. At this moment the external loads were transferred through two compression fields towards the two asperities. These compression fields were delimited by the crack shown in Fig. 15. Because the two asperities in the U-16°-D-37°-T sample prevented movement of the concrete body along the interface to different degrees (as shown by the

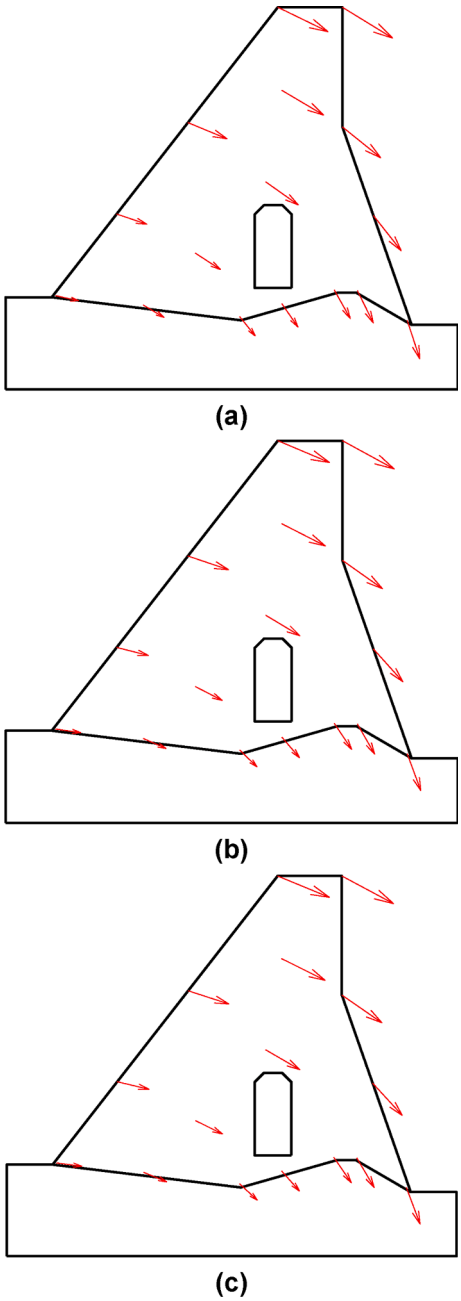

Fig. 16. Displacement vectors for the sample D-16°-F at (a) 75% of hydrostatic load (b) 89% of hydrostatic load and (c) 92% of hydrostatic load.

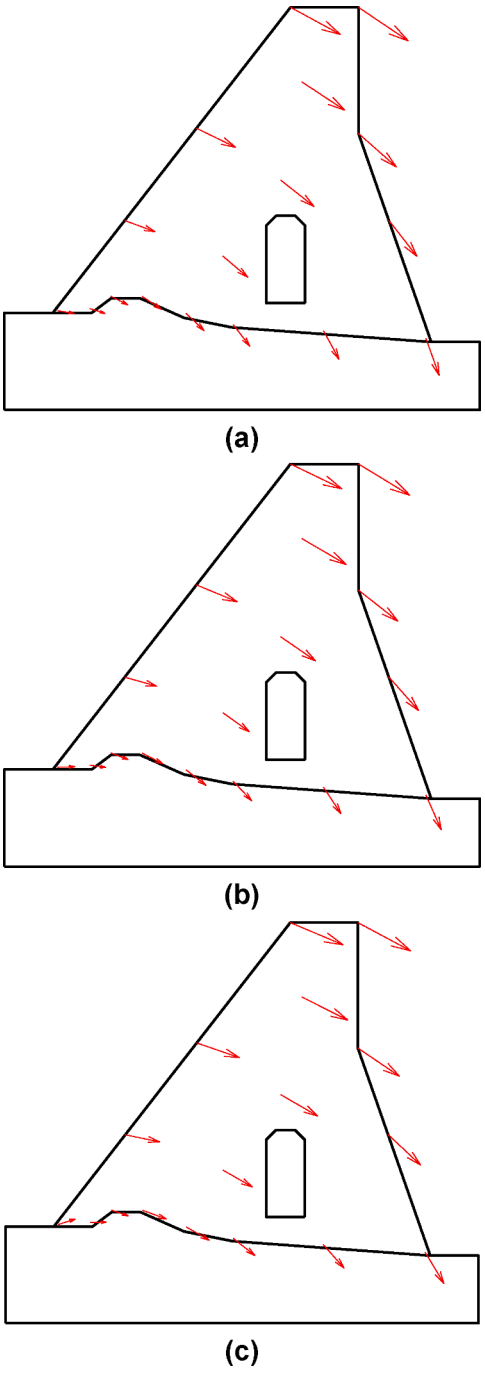

Fig. 17. Displacement vectors for the sample U-37°-F at (a) 75% failure; (b) 90% failure and (c) 100 % failure load.

vectors' directions in Fig. 14), the samples started to exhibit sliding-rotational behaviour. This is in sharp contrast to the movement in the D-37°-T and U-16-T samples, which was rotationally dominated around the single asperity (Fig. 12 and Fig. 20) and sliding dominated (Fig. 11), respectively. As the load increased, the concrete body above the crack in the U-16°-D-37°-T sample rotated with a different gradient from the one below, thus straining the concrete in opposite directions until a tensile crack formed between the two compression fields.

The results of the FEM simulation of the sample U-37°-D-16°-F, confirms the assumption that the shape of the first asperity decisively influence the total behaviour of the sample. Similar to the U-37°-F sample, the steep asperity located upstream generates an interlocking effect. However, in the case of U-37°-D-16°-F sample, the presence of the second asperity allows for the total force to be transferred through a second compressed band therefore redistributing stresses towards the downstream asperity and thus delaying the formation of the crack which in the end is similar to the one observed in the U-37°-F sample (Fig. 19).

5.4. Safety factor from analytical calculations vs model test

The safety factor against sliding of the pillar at the design hydrostatic load without accounting the contribution of asperities, as in LEM would be just 0.47. However, if the full geometry is considered (as in the U-16°-D-37°-T sample) it would be 4. Furthermore, from the results of laboratory tests and FEM, idealized M−C parameters were back-calculated for the samples. Since the pillar and foundation were unbonded, cohesion was assumed to be zero, so only the mobilized friction angle was calculated (Table 3). The mobilized friction angle obtained for R-T was

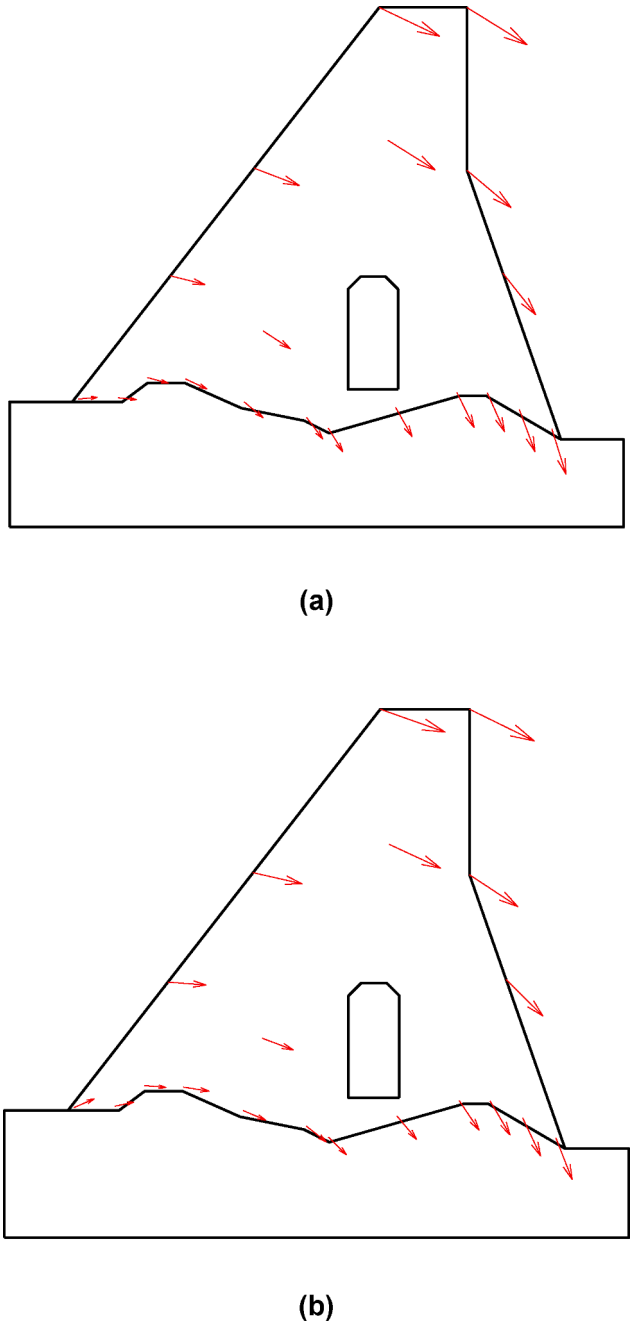

Fig. 18. Displacement vectors for the sample U-37-D-16-F at (a) 100% hydrostatic load and (b) 190% hydrostatic load.

45.6°, while corresponding angles of the samples with asperities ranged between 52° and 61°. The M−C idealization of the results suggests that neglecting asperities at the interface could result in underestimation of the dam's shear capacity. Furthermore, the failure mode, which is influenced by the inclinations and locations of asperities, is not reflected in the M−C parameters.

5.5. Practical applications

The model test method can be used as a stand-alone method for assessing pillars' stability. However, it will be most beneficial for dam stability analysis if the results are benchmarked and used to parameterize numerical modelling. It can also account for effects of 'favourable' factors, such as presence of anchor bolts, plate extensions in man-made trenches in bedrock, reinforcement, deviations from linearity of the interface, and cohesion. Moreover, the 'unfavourable' effects of damage due to accidents, existing cracks due to freeze–thaw cycles, corrosion in reinforcement or damage due to alkali-silica reaction can also be covered.

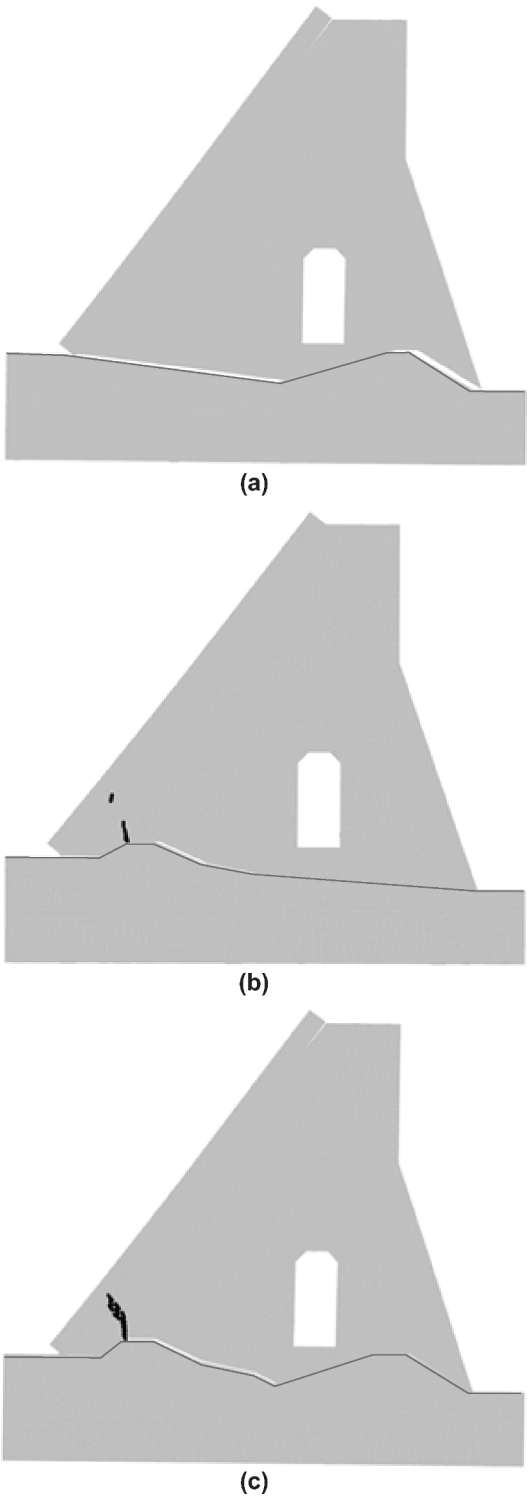

Fig. 19. Failure modes of the FE models with swapped asperity (a) D-16°-F; (b) U-37°-F and (c) U-37°-D-16°-F.

5.6. Limitations of the study

Restricting the tests to pillars, and not including the plate (implicitly treating it as a negligible constant) could have resulted in some

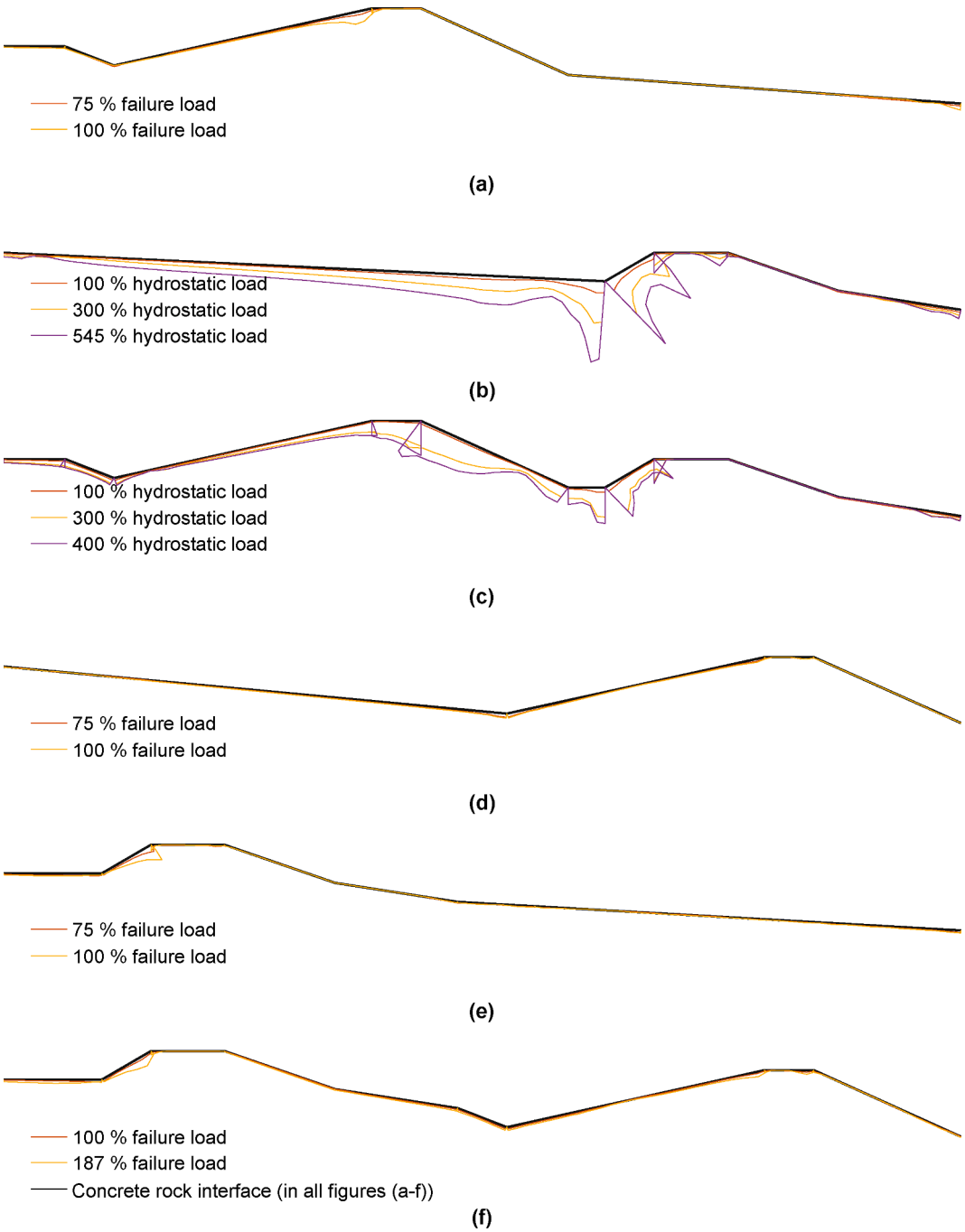

Fig. 20. Compression strains obtained from the numerical analysis of each sample's interface at indicated loading stages (a) U-16-F (b) D-37-F (c) U-16-D-37-F (d) D-16-F (e) U-37-F (f) U-37-D-16-F (loading direction is from left to right, strain magnified by a factor 10 5 for (a)-(f)).

deviations from the true failure mode. For example, the extra weight provided by the plate would increase the normal stresses and the uplift pressure acting on the plate would increase the destabilizing forces, thus potentially influencing the trajectory of the principle stresses. Hence, further studies should include similar tests with plates, and/or numerical modelling to predict the behaviour of systems with plates.

The material parameters should also be varied in model tests to assess associated variations in the body of the dam. As Table 2 shows, the secant modulus are higher than the target values for the model material, therefore it is reasonable to assume that also the shear modulus of the material is also higher than it should be. Hence, the model materials used in the tests have a higher capacity in shear than if the material properties had been scaled perfectly. The scope of this paper is to study how the asperities affect the load capacity of the pillar and not to scale the results directly to the real world therefore these distortion in the material properties are considered to be within reason. Furthermore, the failure mode is not affected by distortion in the material parameters [53]. More work is needed to reduce the distortion in the material properties if the test setup should be used to directly check the load capacity of a pillar.

A shallow foundation was used for the models and it does not contain rock joints as in a rock mass. This could affect the stiffness of the foundation and potentially the failure mode. Hence, further studies should include tests/numerical models with the representation of the rock mass.

6. Conclusions and future work

The objective of the presented work was to characterise effects of large-scale asperities on the shear strength of the unbonded concrete rock interface of a plate dam. Results of the presented experimental tests on model samples and numerical simulations show that both locations and shapes of large-scale asperities strongly influence the shear strength of a concrete-rock interface of small dams. The results show that relative to a planar interface (i.e. reference case in this study, as used in assessment of concrete dams' sliding stability), the modelled asperities in this study can increase the shear capacity of an interface by up to ten times. Depending on their inclinations against the shear direction along the interface, asperities might act as shear keys, changing the stress flow through the structure, and hence affecting the shear strength of the interface. The interlocking of the pillar in large asperities might also create a failure mode, cracking in concrete, not covered in typical assessment procedures for plate dams. Hence, an appropriate model based on strut and tie or concrete plasticity theories could potentially be adapted from existing models of laterally loaded concrete elements to cover this failure mode.

Tests also showed that it is difficult to detect sliding, therefore characteristics of the phenomenon in reality in a pillar would be worth investigating with long term monitoring. Although sliding occurred in some tests, the nature of the failure was not ductile as one might expect. Due to the interlocking effects provided by the asperities, sliding failure ended with a sudden release of energy characterized by resettlement of the sample.

An asperity towards the downstream end of an interface contributes more to strength than one positioned upstream. However, as shown experimentally and confirmed through simulations, more asperities do not necessarily mean more strength. Moreover, the results show that the first asperity is dominant and sets 'the tone' of the entire sample's behaviour, by setting the global displacement direction.

The sample replicating pillar 49 from Kalhovd dam had a shear strength seven times greater than the sample where the asperities were not considered. Analysis of any configurations of profiles investigated in this study (apart from the planar reference profile) would indicate that section 49 is stable.

The vector plots showed that the rigid body movement theory is valid for small displacement until the asperities start to be loaded. Thereafter, the directions of the vectors across the pillar are different, so rigid body assumptions are no longer fulfilled.

Declaration of Competing Interest

The authors declare that they have no known competing financial interests or personal relationships that could have appeared to influence the work reported in this paper.

Acknowledgements

The presented research was part of the 'Stable Dams' project funded by the Research Council of Norway (Grant No. 244029).

References

[1] CDA. Dam Safety Guidelines 2007 (2013 edition). Canadian Dam Association; 2013.
[2] CFBR. Recommendations for the justification of the stability of gravity dams. Recommandations pour la justification de la stabilité des barrages-poids. Comité Français des Barrages et Réservoirs 2012:217.
[3] USACE. Stability Analysis of Concrete Structures. Washington D.C.: US Army Corps of Engineers; 2005.
[4] Johansson F, Stille H. A conceptual model for the peak shear strength of fresh and unweathered rock joints. Int J Rock Mech Min Sci 2014;69:31–8.
[5] Ruggeri G, Pellegrini R, Celix MRd, Berntsen M, Royet P, Bettzieche V et al. Sliding safety of existing gravity dams - final report. Technical report, ICOLD European Club. Working group on sliding safety of existing gravity dams.; 2004.
[6] Krounis A, Johansson F, Larsson S. Effects of spatial variation in cohesion over the concrete-rock interface on dam sliding stability. J Rock Mech Geotech Eng 2015;7:659–67.
[7] Patton FD. Multiple Modes of Shear Failure In Rock. 1st international congress of rock mechanics. Lisbon, Portugal: International Society for Rock Mechanics; 1966.
[8] Zhang X, Jiang Q, Chen N, Wei W, Feng X. Laboratory Investigation on Shear Behavior of Rock Joints and a New Peak Shear Strength Criterion. Rock Mech Rock Eng 2016;49:3495–512.
[9] Grasselli G. Shear Strength of Rock Joints Based on Quantified Surface Description. Rock Mech Rock Eng 2006;39:295.
[10] Maksimović M. The shear strength components of a rough rock joint. International Journal of Rock Mechanics and Mining Sciences & Geomechanics Abstracts. 1996;33:769–83.
[11] Barton N, Choubey V. The shear strength of rock joints in theory and practice. Rock Mechanics. 1977;10:1–54.
[12] Schneider HJ. The friction and deformation behaviour of rock joints. Rock Mechanics. 1976;8:169–84.
[13] Yang J, Rong G, Hou D, Peng J, Zhou C. Experimental Study on Peak Shear Strength Criterion for Rock Joints. Rock Mech Rock Eng 2016;49:821–35.
[14] Huang SL, Oelfke SM, Speck RC. Applicability of fractal characterization and modelling to rock joint profiles. International Journal of Rock Mechanics and Mining Sciences & Geomechanics Abstracts. 1992;29:89–98.
[15] Odling NE. Natural fracture profiles, fractal dimension and joint roughness coefficients. Rock Mech Rock Eng 1994;27:135–53.
[16] Kulatilake PHSW, Balasingam P, Park J, Morgan R. Natural rock joint roughness quantification through fractal techniques. Geotech Geol Eng 2006;24:1181.
[17] Mouzannar H, Bost M, Leroux M, Virely D. Experimental Study of the Shear Strength of Bonded Concrete-Rock Interfaces: Surface Morphology and Scale Effect. Rock Mech Rock Eng 2017;50:2601–25.
[18] Thirukumaran S, Indraratna B. A review of shear strength models for rock joints subjected to constant normal stiffness. J Rock Mech Geotech Eng 2016;8:405–14.
[19] Hencher SR, Richards LR. Assessing the Shear Strength of Rock Discontinuities at Laboratory and Field Scales. Rock Mech Rock Eng 2015;48:883–905.
[20] Haberfield CM, Seidel JP. Some recent advances in the modelling of soft rock joints in direct shear. Geotech Geol Eng 1999;17:177–95.
[21] Fell R, MacGregor P, Stapledon D, Bell G, Foster M. Geotechnical Engineering of Dams. CRC Press; 2005.
[22] Donnelly SRR. Assessment of Shear Resistance for Blasted Rock Foundations. The Canadian Dam Association's 2007 annual conference. Canada: Canadian Dam Association; 2007.
[23] Hencher S, Toy J, Lumsden A. Scale dependent shear strength of rock joints. Scale effects in rock masses 93. 1st Edition ed: CRC Press; 1993. p. 233–40.
[24] Bandis S, Lumsden AC, Barton N. Experimental studies of scale effects on the shear behaviour of rock joints. Int J Rock Mech Min Sci 1981;18:1–21.
[25] Donnelly CR, J Rigbey S. Concepts of Shear Resistance and Practical Applications. HG Acres Annual Seminar. Ontario1998.
[26] Barton N, Bandis S. Review of predictive capabilities of JRC-JCS model in engineering practice. Inernational symposium on Rock Joints. Leon: A A Balkema 1990:603–10.
[27] Barton N, Bandis S. Effects Of Block Size On The Shear Behavior Of Jointed Rock. The 23rd US Symposium on Rock Mechanics (USRMS). California: American Rock Mechanics Association; 1982.
[28] Ladanyi B, Archambault G. Simulation of shear behavior of a jointed rock mass. Proceedings of the 11th Symposium on Rock Mechanics. 1970:105-25.
[29] Papaliangas TT, Hencher SR, Lumsden ACA. Comprehensive Peak Shear Strength Criterion For Rock Joints. 8th ISRM Congress. Tokyo, Japan: International Society for Rock Mechanics and Rock Engineering; 1995. p. 8.
[30] Johansson F. Influence of scale and matedness on the peak shear strength of fresh, unweathered rock joints. Int J Rock Mech Min Sci 2015;82:36–47.
[31] Hack R, Price D, Rengers N. A new approach to rock slope stability – a probability classification (SSPC). Bull Eng Geol Environ 2003;62:167–84.
[32] Palmstrøm A. Characterizing rock masses by the RMi for use in practical rock engineering: Part 1: The development of the Rock Mass index (RMi). Tunn Undergr Space Technol 1996;11:175–88.
[33] Saichi T, Renaud S, Bouaanani N, Miquel B. Effects of Rock Foundation Roughness on the Sliding Stability of Concrete Gravity Dams Based on Topographic Surveys. J Eng Mech 2019;145.
[34] Bista D, Sas G, Johansson F, Lia L. Influence of location of large-scale asperity on shear strength of concrete-rock interface under eccentric load. J Rock Mech Geotech Eng 2020;12:449–60.
[35] NVE. Retningslinjer for betongdammer. Norges Vassdrags- og Energidirektorat; 2005.
[36] Sas G, Seger A, Bista D, Popescu C, Arntsen B. Stable Dams: Capacity and Resistance. Deliverable. Norway: Northern Research Institute Narvik (NORUT Narvik); 2019. p. 118.
[37] Harris HG, Sabnis GM. Structural Modeling and Experimental Techniques. 2nd ed. Boca Raton, Florida: CRC Press; 1999.
[38] Barpi F, Valente S. Numerical simulation of prenotched gravity dam models. J Eng Mech 2000;126:611–9.

[39] Liu J, Feng X-T, Ding X-L, Zhang J, Yue D-M. Stability assessment of the Three-Gorges Dam foundation, China, using physical and numerical modeling—Part I: physical model tests. Int J Rock Mech Min Sci 2003;40:609–31.
[40] Harris DW, Travers F. Investigation of the Failure Modes of Concrete Dams—Physical Model Tests.: U.S. Department of the Interior Bureau of Reclamation; 2006.
[41] Zhu H-H, Yin J-H, Dong J-H, Zhang L. Physical modelling of sliding failure of concrete gravity dam under overloading condition. Geomechanics & engineering. 2010;2:89–106.
[42] Chen Y, Zhang L, Yang B, Dong J, Chen J. Geomechanical model test on dam stability and application to Jinping High arch dam. Int J Rock Mech Min Sci 2015;1–9.
[43] Grøneng G, Nilsen B. Procedure for determining input parameters for Barton-Bandis joint shear strength formulation. Trondheim: Department of Geology and Mineral Resources Engineering, NTNU; 2009.
[44] Baqersad J, Poozesh P, Niezrecki C, Avitabile P. Photogrammetry and optical methods in structural dynamics – A review. Mech Syst Sig Process 2017;86:17–34.
[45] Gmbh GOM. ARAMIS - 3D Motion and Deformation Sensor. GOM 2017.
[46] Červenka V, Jendele L, Červenka J. ATENA Program Documentation Part 1 - Theory. Prague,Czech Republic: Červenka Consulting s.r.o.; 2018.
[47] Richard M, Anders A. Cracking of Concrete Buttress Dam Due to Seasonal Temperature Variation. ACI Struct J 2011;108:13.
[48] Pan T, Wang L, Tutumluer E. Experimental investigation of aggregate-mortar interface affecting the early fracture toughness of Portland cement concrete. Int J Pavement Res Technol 2011;4:168–75.
[49] B2Bmetal.eu. HEA (IPBL) Beams, European standard wide flange h beams, dimensions, specifications. He a beams in accordance with former standard Euronorm 53-62. 2019.
[50] Gu XF, Seidel JP, Haberfield CM. Direct Shear Test of Sandstone-Concrete Joints. Int J Geomech 2003;3:21–33.
[51] Johnston IW, Lam TSK. Shear Behavior of Regular Triangular Concrete/Rock Joints—Analysis. Journal of Geotechnical Engineering. 1989;115:711–27.
[52] Ghazvinian AH, Taghichian A, Hashemi M, Mar'Ashi SA. The Shear Behavior of Bedding Planes of Weakness Between Two Different Rock Types with High Strength Difference. Rock Mech Rock Eng 2010;43:69–87.
[53] Ulfberg A, Seger A, Bista D, Das O, Sas G. Influence of concrete's mechanical properties on the cracking of concrete dams. 31st European Safety and Reliability Conference. Angers, France: European Safety and Reliability Association (ESRA); 2021.